Surface-emitting distributed feedback terahertz quantum-cascade lasers in metal-metal waveguides

Sushil Kumar, Benjamin S. Williams, Qi Qin, Alan W. M. Lee, and Qing Hu

Department of Electrical Engineering and Computer Science and Research Laboratory of Electronics, Massachusetts Institute of Technology, Cambridge, Massachusetts 02139

qhu@mit.edu

John L. Reno

Sandia National Laboratories, Center of Integrated Nanotechnologies, MS 1303, Albuquerque, NM 87185-1303

Abstract:
Single-mode surface-emitting distributed feedback terahertz quantum-cascade lasers operating around 2.9 THz are developed in metal-metal waveguides. A combination of techniques including precise control of phase of reflection at the facets, and use of metal on the sidewalls to eliminate higher-order lateral modes allow robust single-mode operation over a range of approximately 0.35 THz. Single-lobed far-field radiation pattern is obtained using a π phase-shift in center of the second-order Bragg grating. A grating device operating at 2.93 THz lased up to 149 K in pulsed mode and a temperature tuning of 19.7 GHz was observed from 5 K to 147 K. The same device lased up to 78 K in continuous-wave (cw) mode emitting more than 6 mW of cw power at 5 K. In general, maximum temperature of pulsed operation for grating devices was within a few Kelvin of that of multi-mode Fabry-Perot ridge lasers.

© 2007 Optical Society of America

OCIS codes: (140.3070) Infrared and far-infrared lasers; (140.5960) Semiconductor lasers; (140.3490) Distributed-feedback lasers; (250.7270) Vertical emitting lasers.

References and links

1. R. Köhler, A. Tredicucci, F. Beltram, H. E. Beere, E. H. Linfield, A. G. Davies, D. A. Ritchie, R. C. Iotti, and F. Rossi, "Terahertz semiconductor-heterostructure laser," Nature **417**, 156 (2002).
2. G. Scalari, C. Walther, J. Faist, H. Beere, and D. Ritchie, "Electrically switchable, two-color quantum cascade laser emitting at 1.39 and 2.3 THz," Appl. Phys. Lett. **88**, 141102 (2006).
3. A. Lee, Q. Qin, S. Kumar, B. S. Williams, Q. Hu, and J. L. Reno, "Real-time terahertz imaging over a standoff distance ($>$ 25 m)," Appl. Phys. Lett. **89**, 141125 (2006).
4. J. R. Gao, J. N. Hovenier, Z. Q. Yang, J. J. A. Baselmans, A. Baryshev, M. Hajenius, T. M. Klapwijk, A. J. L. Adam, T. O. Klaassen, B. S. Williams, S. Kumar, Q. Hu, and J. L. Reno, "A terahertz heterodyne receiver based on a quantum cascade laser and a superconducting bolometer," Appl. Phys. Lett. **86**, 244104 (2005).
5. H.-W. Hübers, S. G. Pavlov, A. D. Semenov, R. Köhler, L. Mahler, A. Tredicucci, H. E. Beere, D. A. Ritchie, and E. H. Linfield, "Terahertz quantum cascade laser as local oscillator in a heterodyne receiver," Opt. Express **13**, 5890 (2005), http://www.opticsexpress.org/abstract.cfm?URI=OPEX-13-15-5890.
6. A. Lee, B. S. Williams, S. Kumar, Q. Hu, and J. L. Reno, "Real-Time Imaging Using a 4.3-THz Quantum Cascade Laser and a 320 x 240 Microbolometer Focal-Plane Array," IEEE Photon. Technol. Lett. **18**, 1415 (2006).

---

7. B. S. Williams, S. Kumar, H. Callebaut, Q. Hu, and J. L. Reno, "Terahertz quantum-cascade laser at $\lambda \approx 100 \, \mu$m using metal waveguide for mode confinement," Appl. Phys. Lett. **83**, 2124 (2003).

8. B. S. Williams, S. Kumar, Q. Hu, and J. L. Reno, "Operation of terahertz quantum-cascade lasers at 164 K in pulsed mode and at 117 K in continuous-wave mode," Opt. Express **13**, 3331 (2005), http://www.opticsexpress.org/abstract.cfm?URI=OPEX-13-9-3331 .

9. S. Kohen, B. S. Williams, and Q. Hu, "Electromagnetic modeling of terahertz quantum cascade laser waveguides and resonators," J. Appl. Phys. **97**, 053106 (2005).

10. A. J. L. Adam, I. Kašalynas, J. N. Hovenier, T. O. Klaassen, J. R. Gao, E. E. Orlova, B. S. Williams, S. Kumar, Q. Hu, and J. L. Reno, "Beam patterns of terahertz quantum cascade lasers with subwavelength cavity dimensions," Appl. Phys. Lett. **88**, 151105 (2006).

11. B. S. Williams, S. Kumar, Q. Hu, and J. L. Reno, "High-power terahertz quantum-cascade lasers," Electron. Lett. **42**, 89 (2006).

12. D. Hofstetter, J. Faist, M. Beck, and U. Oesterle, "Surface-emitting 10.1 μm quantum cascade distributed feedback lasers," Appl. Phys. Lett. **75**, 3769 (1999).

13. C. Pflügl, M. Austerer, W. Schrenk, S. Golka, G. Strasser, R. P. Green, L. R. Wilson, J. W. Cockburn, A. B. Krysa, and J. S. Roberts, "Single-mode surface-emitting quantum-cascade lasers," Appl. Phys. Lett. **86**, 211102 (2005).

14. M. K. Gunde and M. Maček, "Infrared Optical Constants and Dielectric Response Functions of Silicon Nitride and Oxynitride Films," Phys. Stat. Sol. (a) **183**, 439 (2001).

15. S. Li, G. Witjaksono, S. Macomber, and D. Botez, "Analysis of surface-emitting second-order distributed feedback lasers with central grating phaseshift," IEEE J. Sel. Top. Quantum Electron. **9**, 1153 (2003).

16. S. Kumar, B. S. Williams, Q. Hu, and J. L. Reno, "First-order edge-emitting and second-order surface-emitting distributed feedback terahertz quantum cascade lasers," presented at the 8th International Conference on Intersubband Transitions in Quantum Wells, Cape Cod, Massachusetts, 11–16 Sept. 2005 .

17. O. Demichel, L. Mahler, T. Losco, C. Mauro, R. Green, A. Tredicucci, J. Xu, F. Beltram, H. E. Beere, D. A. Ritchie, and V. Tamošinuas, "Surface plasmon photonic structures in terahertz quantum cascade lasers," Opt. Express **14**, 5335 (2006), http://www.opticsexpress.org/abstract.cfm?URI=OPEX-14-12-5335 .

18. R. J. Noll and S. H. Macomber, "Analysis of grating surface emitting lasers," IEEE J. Quantum Electron. **26**, 456 (1990).

19. N. Finger, W. Schrenk, and E. Gornik, "Analysis of TM-polarized DFB laser structures with metal surface gratings," IEEE J. Quantum Electron. **36**, 780 (2000).

20. M. Schubert and F. Rana, "Analysis of Terahertz Surface Emitting Quantum-Cascade Lasers," IEEE J. Quantum Electron. **42**, 257 (2006).

21. B. S. Williams, S. Kumar, Q. Hu, and J. L. Reno, "Distributed-feedback terahertz quantum-cascade lasers with laterally corrugated metal waveguides," Opt. Lett. **30**, 2909 (2005).

22. J. Jin, *The Finite Element Method in Electromagnetics*, 2nd ed. (Wiley-IEEE Press, 2002).

23. R. Williams, *Modern GaAs processing methods*, chapter 5, p. 97, 2nd ed. (Artech House, Boston, 1990).

24. M. A. Ordal, R. J. Bell, R. W. Alexander-Jr., L. L. Long, and M. R. Querry, "Optical properties of fourteen metals in the infrared and far infrared: Al, Co, Cu, Au, Fe, Pb, Mo, Ni, Pd, Pt, Ag, Ti, V, and W," Appl. Opt. **24**, 4493 (1985).

1. Introduction

Terahertz (THz) quantum-cascade lasers (QCLs) have been developed rapidly covering the frequency range of 1.39–4.9 THz ($\lambda \sim 215 - 60 \, \mu$m) since their advent in 2001 [1, 2, 3]. These lasers are expected to find applications as local oscillators for heterodyne receivers or as sources for imaging and spectroscopy [4, 5, 6]. Stable continuous-wave (cw) single-mode emission is required for local oscillators and several milliwatts of optical power in a narrow beam is desired to obtain large dynamic range and high-spatial resolution in an imaging system. Additionally, some applications may have stringent frequency requirements either to target a particular spectroscopic feature or to avoid certain atmospheric water absorption bands.

The radiation and frequency characteristics of a laser are largely dependent on the waveguide design, which, for THz QCLs, has provided challenges at par with those of the active region design itself. The best QCLs in terms of high temperature operation have been demonstrated in the so-called metal-metal (MM) waveguides that are essentially microstrip transmission lines commonly used at microwave frequencies [7, 8]. In addition to having a low waveguide loss α_w in the terahertz, MM waveguides provide strong mode confinement due to sub-wavelength mode localization in vertical dimension, resulting in high facet-reflectivities and a mirror loss

$\alpha_{\mathrm{m}} \ll \alpha_{\mathrm{w}}$ [9]. However, their efficient waveguiding comes at the price of a severe mode mismatch between the waveguided and the free-space radiation modes. As a result, light emission from edge-emitting Fabry-Perot ridge waveguides is highly divergent [10], output power is low, and higher-order modes in the lateral (width) dimension are often excited even in narrow ($< 50\,\mu$m) waveguides. The other type of waveguides often used for THz QCLs are the semi-insulating surface-plasmon (SISP) waveguides that provide greater output power and tighter beam patterns but are limited in their temperature performance due to higher threshold current densities [1, 5, 11]. This higher threshold current density, even using long waveguide structures (> 4 mm), is likely due to additional waveguide losses that result from the large fraction of the mode propagating outside the gain medium. The impurity absorption in the semi-insulating substrate, which occur at THz frequencies for shallow donors and acceptors, could contribute significantly to waveguide losses for low confinement factors.

The objective of this work is to preserve the advantage of the metal-metal waveguide structures, but increase the output power levels and improve the beam patterns. For this purpose, it is instructive to analyze the effect of two waveguide parameters, the waveguide loss α_{w} and the facet (mirror) loss α_{m}, on the lasing threshold (and therefore the maximum operating temperature) and the output power levels. To a leading degree, the lasing threshold is proportional to $(\alpha_{\mathrm{w}}+\alpha_{\mathrm{m}})/\Gamma$, where Γ is the mode confinement factor and ≈ 1 for the MM waveguides. On the other hand, the output power is proportional to the slope efficiency, which is proportional to the factor $\alpha_{\mathrm{m}}/(\alpha_{\mathrm{w}}+\alpha_{\mathrm{m}})$. Because of the high facet reflectivity [9], the mirror loss is low in the MM waveguides, $\alpha_{\mathrm{m}} \approx 1$ cm^{-1} in comparison to the waveguide loss $\alpha_{\mathrm{w}} \approx 10$ cm^{-1}. This analysis indicates that by increasing the facet loss, we will be able to increase the output power levels proportionally, but will increase the lasing threshold only marginally as long as $\alpha_{\mathrm{m}} < 5$ cm^{-1}. In microwave engineering, this increase of the facet loss (or the output coupling efficiency) is usually done by using a tapered mode matching structure to adiabatically transform the low impedance of the microstrip transmission line to the free-space impedance. At the output of the mode matching structure, the cross section is much greater than the wavelength, resulting in a much tighter far-field beam pattern. In principle, such a technique could be applied here to the MM waveguide THz lasers. However, because of the shorter wavelengths at THz frequencies, the fabrication and assembly of such mode-matching structures will be quite demanding.

An alternative method to increase the mirror loss is by using a second-order distributed feedback (DFB) grating to couple the laser beam out from the surface. The output coupling loss α_{m} can be increased in a controllable way by choosing the grating duty cycle, phase of reflection at facets, and a central defect. A large surface area for emission provides the possibility of an improved beam pattern in addition to higher optical power levels. Furthermore, the DFB nature of this structure allows robust single-mode operation and frequency selectivity, which are required for all sensing applications involving narrow target spectral features. High-power surface-emitting quantum-cascade lasers using second-order DFB gratings have been well developed at mid-infrared frequencies [12, 13]. However, implementation of such gratings in MM waveguides at THz frequencies turned out to be much more challenging because of mode competition from strongly confined higher-order lateral modes and high reflection from end-facets of the cavity (reflectivity ~ 0.7–0.9) [9]. At mid-infrared frequencies, silicon-nitride that is used to cover the side walls for electrical isolation, strongly absorbs radiation [14]. This, in addition to the fact that higher-order lateral modes have a greater overlap with the lossy doped cladding layers, effectively eliminated all such modes by accident or design. At THz frequencies, the absorption by the insulator (silicon-nitride or silicon-dioxide) is much weaker, and higher lateral modes are easily excited due to strong mode confinement in MM waveguides. As discussed below, new methods are needed to develop surface-emitting THz quantum-cascade lasers with the desired grating modes in such waveguides.

In this paper, we report the design and fabrication techniques to eliminate higher-order lateral modes and to control the phase of reflection at the facets so that it does not interfere with DFB operation. Control of the facet-phase also allows engineering of the mode-shape for the excited mode to minimize possibility of longitudinal spatial-hole burning that can cause multiple-mode behavior at high-bias conditions. In these devices, robust single-mode operation is demonstrated under all bias-conditions at frequencies over a range of ~ 0.35 THz centered around 2.9 THz for a set of devices with various grating periods. A single-lobed far-field radiation pattern is achieved using a π phase-shift in center of the grating [15, 16]. In pulsed operation, the grating device lasing near the peak frequency of the gain spectrum lased up to 149 K, while the grating device operating away from the gain peak still lased up to 141 K. In comparison, multi-mode Fabry-Perot ridge structures on the same die lased up to 153 K, thus demonstrating a relatively small degradation in temperature performance from the implementation of surface-gratings. The measured cw power level, ~ 6 mW, is ~ 2 times higher than that measured from a single facet of edge-emitting lasers with a comparable area.
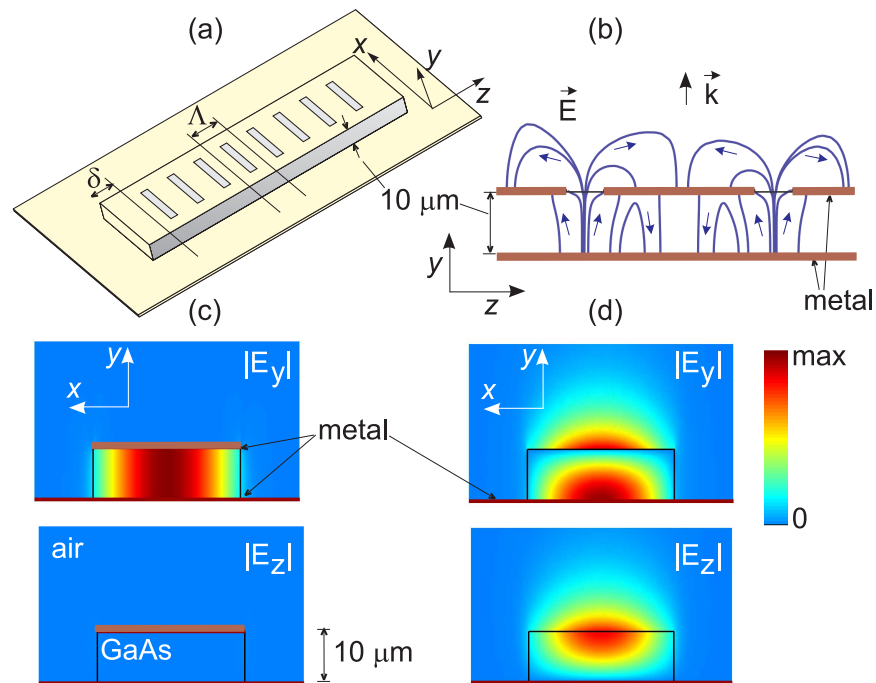

Fig. 1. (a) Three dimensional schematic of the grating structure. (b) Electric-field lines for a grating mode showing the grating induced change in field polarization to achieve surface emission. (c),(d) Electric-field profiles for the fundamental propagating mode in an infinitely long, 100 μm wide waveguide with and without top-metal, respectively, at 3 THz. The corresponding propagation mode indices n_{eff} are 3.58 and 2.66 where n_{GaAs} is taken to be 3.6. The aspect ratio for the plotted geometry in the x and y directions is not to scale.

2. Grating design

While metallic gratings for surface emission have been demonstrated in SISP waveguides [17], the design, analysis, and operation of such gratings is considerably different for MM waveguides. Figure 1(a) shows our scheme for implementing second order DFB in MM waveguides [16]. The 10 μm thick GaAs/Al$_{0.15}$Ga$_{0.85}$As multiple-quantum well (MQW) gain

region is sandwiched between metal on top and bottom. Due to intersubband polarization selection rule, in order to couple with the material gain, the electric field must be polarized normal to the MQW layers. Hence, for unpatterned Fabry-Perot ridge lasers electric-field in the mode is vertically polarized and only edge emission is possible. However, as shown in Fig. 1(b), field polarization could be "bent" by having apertures in the top-metal. The thin highly doped GaAs contact layer, which is often used at the top of the MQW stack to facilitate electrical contact, must be removed from the aperture regions so that it will not cause a significant cavity loss due to the presence of E_z field in apertures. For a second-order Bragg grating with grating-period Λ the same as the wavelength of propagating mode inside the semiconductor ($\approx \lambda_{GaAs} \sim 28\ \mu$m at 3 THz), the grating acts like a phased-array antenna and the E_z fields in all the apertures are in phase to produce vertical emission. Additionally, such a grating provides a strong feedback into the cavity for DFB action.

The standard coupled-mode theory is no longer applicable for such a grating due to sub-wavelength mode confinement in the vertical direction. This can be seen from propagating mode solutions for structures with and without top-metal as shown in Fig. 1(c), and Fig. 1(d). There is a large difference in the mode-shapes for the two cases, which causes a strong mode-mismatch at each grating step. Thus numerical analysis is necessary to understand DFB operation. As will be explained below, grating operation depends critically on the end-length δ which sets the phase of reflection at the facets. The facets are high-reflectivity (HR) coated to prevent edge-emission, which is highly divergent and can couple back into the cavity externally to interfere with grating modes [9].

Propagating mode solutions for an infinite-length periodic grating structure can be found numerically as the Floquet-Bloch eigen-modes [18, 19, 20]. When the propagation wavevector $2\pi n_{eff}/\lambda_0$ equals the Bragg wavevector $2\pi/\Lambda$, the mode is in resonance with the grating and two standing wave solutions exist, each at two slightly different frequencies, thus forming a bandgap at resonance. This is analogous to the energy splitting at Brillouin-zone boundary for electronic dispersion in a periodic lattice. For propagation vectors close to $2\pi/\Lambda$, the modes of a finite-length DFB structure could be written as a linear superposition of the two resonant band-edge modes of the infinite-length grating, each multiplied by slowly-varying envelopes along the length of the grating [20]. This is a good approximation so long as the envelopes do not change rapidly over a distance of Λ. This approximation will, however, break down for small cavities or for highly localized modes that can exist for some specific boundary conditions.

We have performed finite-element (FEM) simulations to analyze grating operation using a commercially available software (FEMLAB 3.1, Comsol Inc.) [21]. FEM simulations were especially useful to understand grating behavior in finite-length structures for different boundary conditions (with and without HR-coated facets) and with additional aperiodicity added in the center of the gratings. A complex eigenfrequency solver was used to solve the electromagnetic eigenvalue problem formulated by surrounding the grating structure with lossy absorbing regions. To compute surface-loss only, both metal and active region were taken to be lossless. For an eigenmode solution with a complex eigenfrequency $\omega_{complex} = \omega_{real} + i\omega_{imag}$, ω_{real} corresponds to resonant frequency of the mode and $2\omega_{imag}n_{GaAs}/c$ corresponds to surface-loss per unit length for mode-intensity inside the waveguide. The challenge lies in the design of boundaries that can absorb radiation isotropically with minimum reflection. For two-dimensional simulations, we implemented an absorbing region by adding a linearly graded imaginary component to the dielectric constant of vacuum as a function of radial distance from the waveguide. For three-dimensional simulations, a standard perfectly-matched layer (PML) with anisotropic permittivity and permeability was implemented and its parameters coarsely adjusted to achieve minimum reflection at THz frequencies [22].

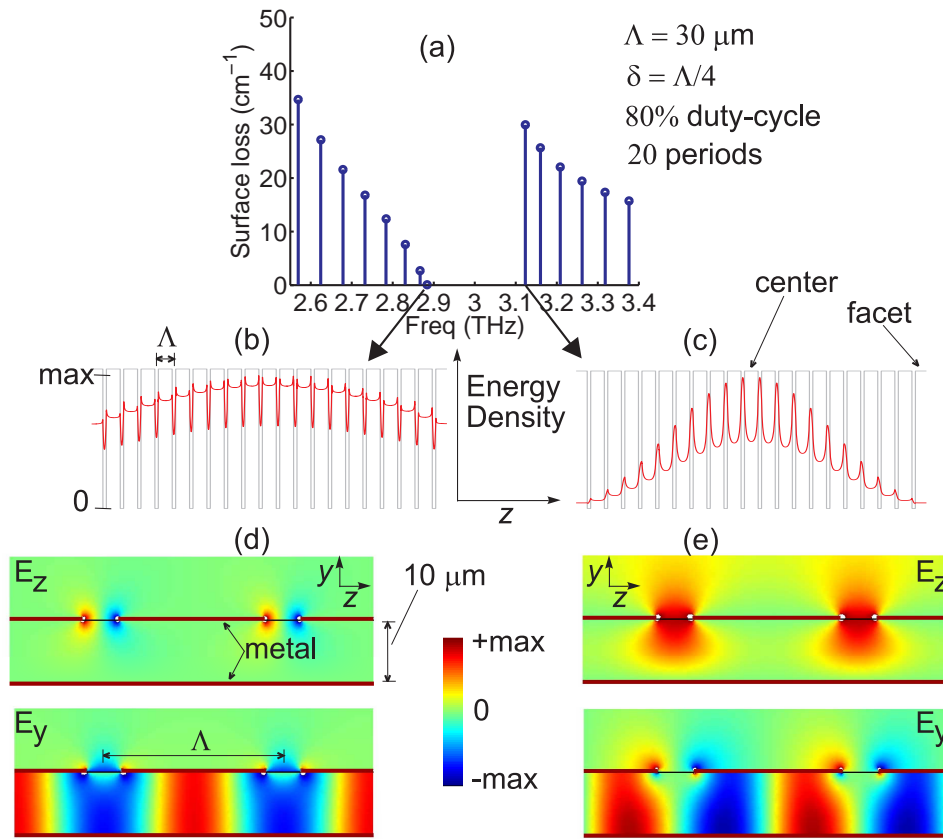The grating mode-spectrum, and mode characteristics for the lower and upper band-edge

Fig. 2. (a) Mode-spectrum for a finite length (infinite-width) grating structure of the type shown in Fig. 1. Plotted is propagation loss inside the waveguide due to surface out-coupling only. (b),(c) Energy-density averaged along waveguide height for lower and upper band-edge modes plotted along the length. The grey rectangular lines are shown as guides to locate grating apertures. (d),(e) Electric-field profiles near center of grating for lower and upper band-edge modes respectively.

modes for a finite-length grating structure with end-lengths $\delta = \Lambda/4$ are shown in Fig. 2. For the lower band-edge mode the energy density is localized more in regions with top-metal. Consequently, the mode character is more like Fig. 1(c), and E_z for this mode is small resulting in negligible surface-loss. Conversely, the upper band-edge mode is localized more under the apertures, and like in Fig. 1(d), can support large E_z in the apertures resulting in greater surface-loss. This also means that the propagation mode index n_{eff} for the upper-band edge mode is smaller since a larger fraction of the mode propagates in air, which is why this mode occurs at a higher frequency. A bandgap of 0.24 THz, which is $\sim 8\%$ of the center frequency, is observed for such a grating indicating very strong DFB action.

For an infinite-length grating the lower band-edge mode is antisymmetric in E_z, which interferes destructively and results in zero radiation loss. However, the upper band-edge mode is symmetric in E_z, which results in constructive interference leading to strong vertical radiation. In a finite-length structure, facets break periodicity of the grating and hence, grating modes acquire a mixed character and a non-uniform envelope shape. For the lower band-edge mode, $|E_y|$ has maxima at centers of the apertures and at middle points between two adjacent apertures,

as shown in Fig. 2(d). Hence, an end-length of $\delta = \Lambda/4$ causes the location of the HR-coated facet to coincide with a null of E_y, thus automatically satisfying the facet boundary condition. This causes least perturbation to the infinite-length lower band-edge mode character and the envelope shape in Fig. 2(b) is relatively uniform along the length. Such an end-length is desired for robust single-mode operation as it minimizes longitudinal spatial-hole burning. However, the highly antisymmetric mode character yields very small surface-loss and low output power.
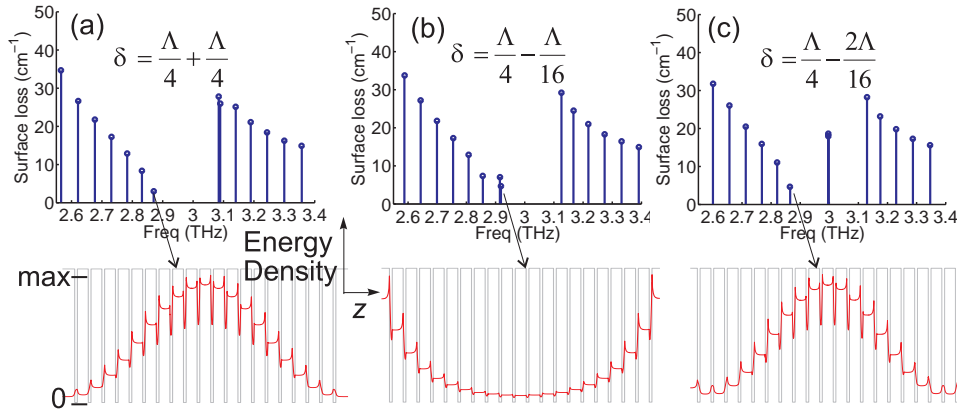
Fig. 3. (a),(b),(c) Grating mode-spectrums and average energy-density plots along waveguide length for the lowest-loss modes corresponding to three different end-lengths. Other grating parameters are the same as in Fig. 2.

Figure 3, along with Fig. 2(a) and Fig. 2(b), capture the importance of facet boundary condition for this type of grating. Mode behavior for a grating will remain mostly unchanged if δ is replaced by $\delta \pm n\Lambda/2$. As the end-length δ is increased from $\Lambda/4$ to $\Lambda/2$, the lower-band edge mode deviates further from that of the infinite-length solution and it acquires a more non-uniform mode shape and a greater surface-loss. For $\delta = \Lambda/2$, the envelope amplitude is zero at the facets (Fig. 3(a)). Figure 3(b) shows the mode-behavior when δ is made less than $\Lambda/4$. Only by slightly reducing δ, two modes that are mostly localized near the facets become the lowest loss modes. Such facet localized modes are not desirable since they will lead to a divergent beam-pattern along the longitudinal (z) direction. For δ further away from $\Lambda/4$ in the negative direction, the facet-localized modes move through the band-gap (as in Fig. 3(c)) and eventually for $\delta = 0$, the mode spectrum is similar to that for $\delta = \Lambda/2$.

E_z for the lower band-edge mode is antisymmetric in z within the grating apertures (Fig. 2(d)). For apertures located symmetrically about the center of a finite length ridge, apertures in one half of the ridge length emit in opposite phase to those in the other half. This causes the envelope for E_z to be antisymmetric along the grating length, as shown in Fig. 4(a). Consequently, the far-field radiation pattern for the lower band-edge mode is predominantly two-lobed with a null in the center. Polarity of the E_z envelopes could be flipped from anti-symmetric to symmetric and vice-versa for all modes by introducing a π phase shift in the grating center by means of a $\pm n\Lambda/2$ defect [15]. This is essentially equivalent to flipping the phase of emission from all apertures in one half of the grating length by π with respect to the other half. The mode-spectrum, energy-density mode-shapes, and grating behavior for different end-lengths essentially remain the same as that of a grating without defect. Figure 4(b) shows one such case, when due to a $-\Lambda/2$ central defect, entire grating emits in phase and a single lobed far-field pattern is obtained with a maxima in the center. Such a radiation pattern is highly desirable for practical applications.
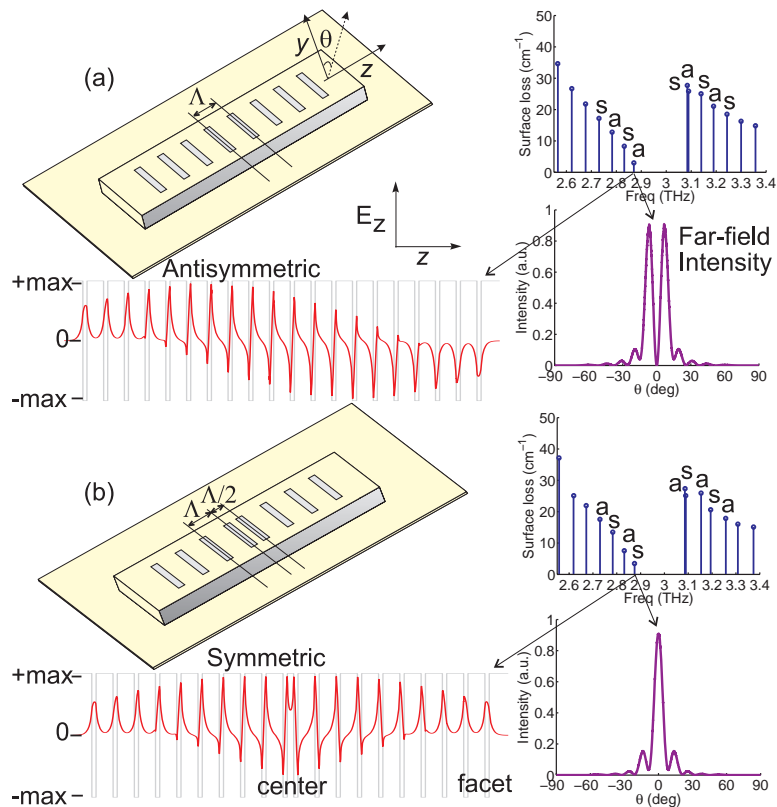
Fig. 4. (a) Grating mode spectrum, and vertically averaged E_z plotted along the length with the corresponding far-field radiation pattern for the lower band-edge mode. These are calculated for end-length $\delta = \Lambda/2$ to show the mode behavior clearly since this δ produces a relatively bigger surface loss. Other grating parameters are the same as in Fig. 2. E_z envelopes are alternately antisymmetric ('a') and symmetric ('s') along the length for adjacent modes. (b) Same quantities plotted for a similar structure that has a $\Lambda/2$ section of waveguide removed from the center to create a $-\Lambda/2$ defect in the grating. Consequently, polarities for E_z envelopes are switched from 'a' to 's' and vice-versa.

3. Early attempts: problems with higher-order lateral modes

In our earlier attempts, grating structures with varying cavity dimensions, grating periods, end-lengths, and grating duty-cycles were fabricated by dry-etching [16]. A 3 THz QCL grown by MBE in GaAs/Al$_{0.15}$Ga$_{0.85}$As, as described in Ref. [8], was used as the gain medium. Wafer bonding for MM waveguide fabrication was done using a copper-to-copper thermocompression technique as detailed in Ref. [8]. After the grating-metal lithography, ridges were defined by reactive-ion etching in a BCl$_3$:N$_2$ plasma with PECVD silicon-nitride used as an etch-mask. While the facets were HR-coated with silicon-nitride/Ti/Au, the sidewalls were left uncoated.

Figure 5(a) shows the scanning-electron micrograph (SEM) of a typical fabricated device. Out of the many devices tested, few lased in single-mode. A spectrum of one such device, that emitted 1.5 mW of cw power at 5 K, is shown in Fig. 5(b). However, the radiation pattern of this device measured using a microbolometer camera showed multiple lobes with a null in the center along the lateral (x) direction, as shown in Fig. 5(c). This beam pattern indicates that the lasing mode is a higher-order lateral mode. The emission frequency for single-mode devices
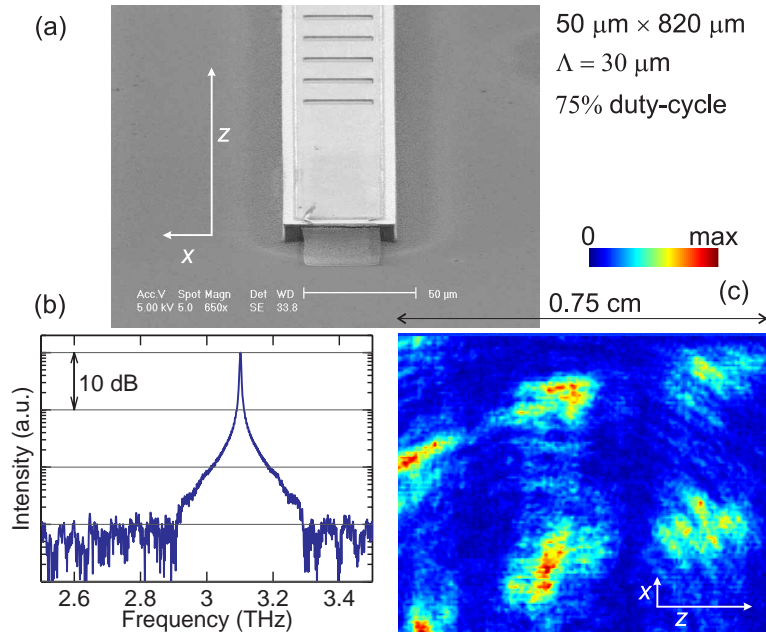
Fig. 5. (a) SEM of a grating device fabricated by dry-etching. (b) Single-mode cw spectrum from one such grating device measured at 5 K. (c) Far-field intensity pattern for the same device measured at a distance of ≈ 2.5 cm with a microbolometer camera [6].

usually did not scale according to the grating-period Λ. These observations suggested that the desired grating mode (with the fundamental lateral mode) was not excited.

Due to the surface-plasmon nature of the modes that are attached to the top and bottom metal plates, MM waveguides provide strong confinement for multiple higher lateral modes. For example, in a 40 μm wide ridge waveguide at 3 THz, modal-confinement for the first two lateral modes is greater than 90 %. For facet-reflectivities that are close to unity, it is quite common experimentally to observe higher-order lateral modes in Fabry-Perot cavities. To investigate the behaviors of the higher-order lateral modes in the grating structures, FEM simulations were done in three-dimensions. Figure 6 shows computed grating mode-spectrum for fundmental and second lateral modes for one such grating. As observed, surface-loss for the second lateral modes in a 40 μm wide waveguide is lower than that of the fundamental modes. Consequently, these modes will reach the lasing threshold first and then gain clamping prevents the device from operating at the desired fundamental modes. For a general grating structure, the lowest-loss modes (due to surface coupling) are the highest-order lateral modes that are supported by the waveguides. For those modes, their longitudinal wavevector k_z becomes much smaller than the total wavevector k_{GaAs} ($= 2\pi n_{GaAs}/\lambda_0$) in the semiconductor due to a significant component k_x along the lateral dimension. For such modes, the surface out-coupling from the grating is much weaker, since E_z is proportional to k_z ($E_z \propto \partial H_x/\partial y \propto k_z \partial E_y/\partial y$) for a given mode intensity inside the waveguide. In general, mode competition from higher lateral modes makes operation of this type of gratings with high-reflectivity at the facets less predictable.

The dry-etching technique used for fabricating these structures is also not without problems. Firstly, nitride coverage on edges of the grating apertures might not be isotropic making the active region in apertures prone to etch-damage. Secondly, the bottom metal surface reached at the completion of dry-etch is rough, making it hard for any bonding pads to stick on it. This puts an additional requirement on the grating to have long end-lengths (as shown in Fig. 5(a)) so
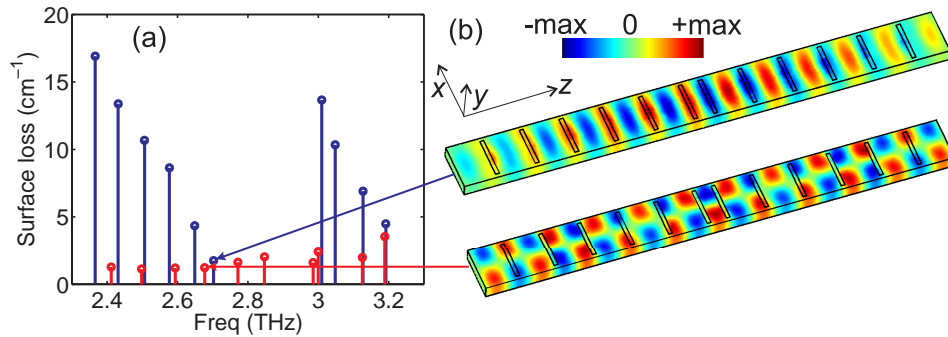
Fig. 6. (a) Grating mode spectrum obtained by three-dimensional simulation of a 12-period grating with $\Lambda = 32\ \mu$m, $\delta = \Lambda/4 + \Lambda/8$, 90 % duty-cycle, and $-\Lambda/2$ defect in center. The cavity facets are covered with metal while the sidewalls are left open. Ridge dimensions are 40 μm $\times$ 392 μm $\times$ 10 μm. Modes in blue are fundamental lateral modes and the ones in red are second lateral modes. (b) E_y plots in the waveguide for the lower band-edge fundamental lateral mode, and for a second lateral mode close to it in frequency.

that electrical contact could be made by wire bonding on top of the mesa. This is not desirable since wire-bonds could pose a strong perturbation to the grating structure due to a significant fraction of the mode that exists near the end facets. The following section describes a modified fabrication process with wet-etching that helps counter the aforementioned problems.

4. Modified design and fabrication

The higher lateral modes can selectively be made more lossy by covering waveguide sidewalls with insulator/metal and extend these layers to bonding pads, as will be described in this section. To do this viably, outward-sloped sidewalls are desirable, which is possible to obtain by wet-etching. Furthermore, wet-etching results in a smooth bottom surface that is better suited for bonding pad fabrication so that wire bonds could be made away from the mesas. For GaAs, the wet-etch profile is usually different in different lattice directions for most reaction-rate limited etchants. Figure 7(a) and Fig. 7(b) show etch profiles in the two different directions obtained typically with H_2SO_4:H_2O_2:H_2O or H_3PO_4:H_2O_2:H_2O etchants for etch masks aligned parallel to the cleave ($\langle 110 \rangle$) directions. For a cavity that needs to be coated with metal on all the sides, the inward slope in Fig. 7(b) will not be suitable for metal patterning by liftoff lithography.

We avoided this problem by aligning the etch mask at $45\,^\circ$ angle to the cleave direction (i.e. along $\langle 100 \rangle$) on the (100) GaAs substrate [23]. Figure 7(c) shows the etch profile obtained with a square shaped etch-mask. Outward-sloped sidewalls are obtained on all four sides. Once the bottom-metal is reached, the mesa could be over-etched to obtain a more vertical side-profile since the bottom of the mesa etches faster compared to the top due to a galvanic effect in the presence of the bottom-metal. For an etch mask with $45\,^\circ$ angle alignment, several H_2O_2 based etchants were tried with H_3PO_4, H_2SO_4, HCl, and NH_4OH in different concentrations. The HCl based etchants caused severe undercut at the bottom of the mesas, while the NH_4OH based etchants damaged the sidewalls making them jagged at several locations. The etch profiles for H_2SO_4 and H_3PO_4 based etchants were very similar, although etching was two to three times faster with H_2SO_4. An etch solution of H_2SO_4:H_2O_2:H_2O 1:8:80 was finally selected for its relatively fast etch-rate ($0.5 - 0.7\ \mu$m/min) and smooth sidewalls.

Sidewall coverage with insulator/metal can selectively make higher lateral modes more lossy for MM waveguides at THz frequencies. The waveguide width is comparable to wavelength, and hence the higher lateral modes can couple to propagating modes in the bonding pad region,
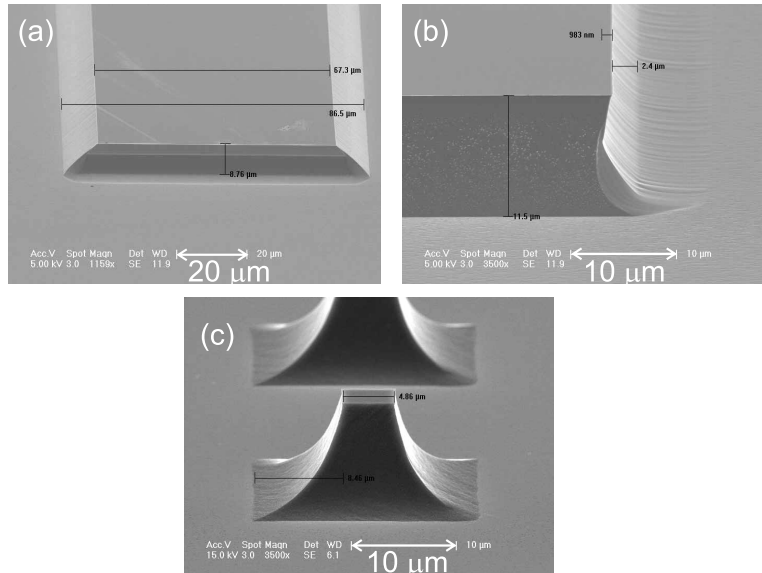
Fig. 7. (a),(b) SEMs of a wet-etched GaAs/Al$_{0.15}$Ga$_{0.85}$As MQW region grown on a (100) GaAs substrate taken along longitudinal and lateral directions, respectively, of a rectangular mesa. Etch-mask for the mesa was aligned parallel to $\langle 110 \rangle$ directions. The bottom surface is GaAs. (c) SEM of a mesa when etch-mask was aligned parallel to $\langle 100 \rangle$ directions. The etchant used was H$_2$SO$_4$:H$_2$O$_2$:H$_2$O 1:8:80 and etch-depth was ≈ 10 μm. The bottom surface is metal.

which is quite lossy since it is essentially a parallel plate waveguide with small plate separation. Figure 8(a) shows propagating mode solutions for an 80 μm wide ridge waveguide covered with 300/30/350 nm of SiO$_2$/Ti/Au on the sidewalls. The active region is taken to be loss less and the metal is approximately modeled with the following Drude parameters: $n_{\text{Ti}} = 4.6 \times 10^{21}$ cm^{-3}, $n_{\text{Au}} = 5.9 \times 10^{22}$ cm^{-3}, and τ for both metals is taken as 50 fs, a value greater by a factor of ~ 2 compared to the published room temperature values [24] (which is justified by the fact that typically for these metals, the published low-frequency mobilities at ~ 100 K are greater by a factor of $2 - 5$ compared to their room temperature values). The extra loss for higher lateral modes is due to bonding-pad regions that could develop high fields at sharp corners, rather than insulator/metal on the sidewalls where field is almost zero. Figure 8(c) shows experimental confirmation of this behavior. An edge-emitting Fabry-Perot laser with insulator/metal on its sidewalls exhibited a spectrum with equal frequency spacing between its modes. From this we infer that the device lased in Fabry-Perot modes corresponding to the fundamental lateral mode. However, a device without metal on its sidewalls had non-uniformly spaced frequencies in its spectrum, which suggests that more than one type of lateral mode was lasing.

5. Results

The techniques outlined in the previous section were implemented and the modified grating devices have performed as expected. Figure 9 shows SEMs of grating devices fabricated by wet-etching with cavity dimensions of 65 μm $\times \sim 0.9$ mm $\times 10$ μm. 30-period gratings with Λ in the range of 28–32 μm were implemented with $\delta \approx \Lambda/4 + 2$ μm, 80 % duty-cycle, and a $-\Lambda/2 - 0.5$ μm defect in the center. The defect was chosen slightly smaller than $-\Lambda/2$ since it reduces the relative amplitude of side-lobes in the far-field pattern of Fig. 4 by apodiz-
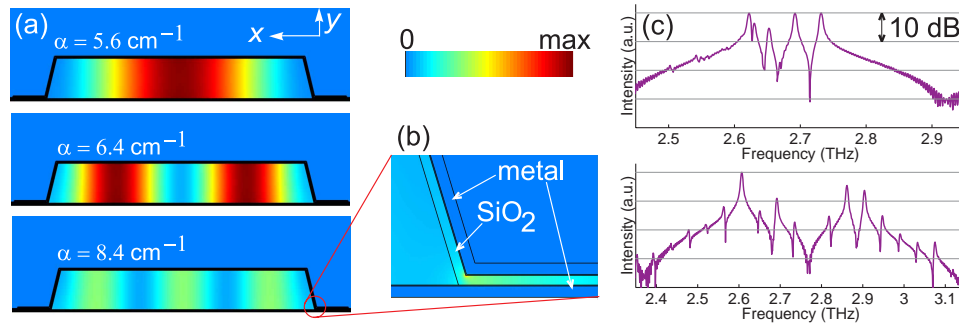
Fig. 8. (a) Energy-density profiles for different lateral modes at 2.9 THz in an 80 μm wide metal-metal waveguide covered with SiO$_2$/Ti/Au on the sidewalls. Calculated propagation loss α due to metal only is indicated. The aspect ratio of the plotted geometry is not to scale. (b) Close-up for the third-lateral mode near the bottom edge of the ridge. (c) Measured cw spectra on log scale at 5 K from two Fabry-Perot ridge lasers with cleaved facets (size 80 μm $\times$ 0.92 mm) located close to each other on the same die. The two devices are nominally identical except the one without metal on the sidewalls yielded higher-order lateral modes (top, where the mode spacing is nonuniform); while the one with metal on the sidewalls yielded only fundamental lateral mode (bottom).

ing the mode shape inside the waveguide. Gratings without a defect were not implemented because of lack of available space on mask. The choice of the end-length δ, as noted previously, predominantly determines the mode-shape for the lasing mode inside the waveguide (Fig. 2(b) and Fig. 3). While $\delta = \Lambda/4$ gives the most uniform mode-shape, the corresponding surface out-coupling is negligible and the mode spectrum depends very sensitively to δ. By increasing δ, surface out-coupling could be increased at the cost of a more non-uniform mode inside the waveguide, which is more prone to longitudinal spatial-hole burning. To achieve the primary purpose of robust single-mode operation, δ in this design was only slightly detuned from $\delta = \Lambda/4$. The choice of a large grating duty-cycle was based more on electrical transport requirements rather than grating operation. A smaller duty-cyle provides greater surface out-coupling; however, due to absence of the highly doped GaAs contact layer in the apertures, current injection becomes more non-uniform. In that situation, different modules of the QCL may be biased differently and push the device into a negative-differential resistance region at an early bias, thereby limiting its lasing dynamic range.

A 2.9 THz QCL active region grown on a (100) GaAs substrate (design FL179C-M9, growth EA1189), very similar in both performance and design to the one described in Ref. [8], was used for fabrication of these grating devices. The fabrication sequence was as follows. The Cu-Cu thermocompression bonding technique as detailed in Ref. [8] was used as a first step towards the MM waveguide fabrication. Following back-substrate removal by lapping and selective etching, the 100-nm thick highly doped top contact GaAs layer, was completely removed by wet-etching. Ti/Au (20/350 nm) metal-gratings were then defined on the 10 μm thick epitaxial active region by contact-lithography, with mask edges aligned along $\langle 100 \rangle$ directions. A second lithography step to cover the grating-metal was performed for the photoresist to be used as a mask for wet-etching of mesas. Wet-etching followed in a H$_2$SO$_4$:H$_2$O$_2$:H$_2$O 1:8:80 solution for $\approx$ 25 minutes. This included a few minute over-etch after all bottom metal was exposed to reduce the slope on the sidewalls and allow for a more uniform current density through the height of the mesa. 300 nm of PECVD silicon-dioxide was then blanket-deposited everywhere at a temperature of 300°C. The next lithography step was to open windows on top of mesas to remove the silicon-oxide by wet-etching in buffered-HF. The final lithography was for Ti/Au
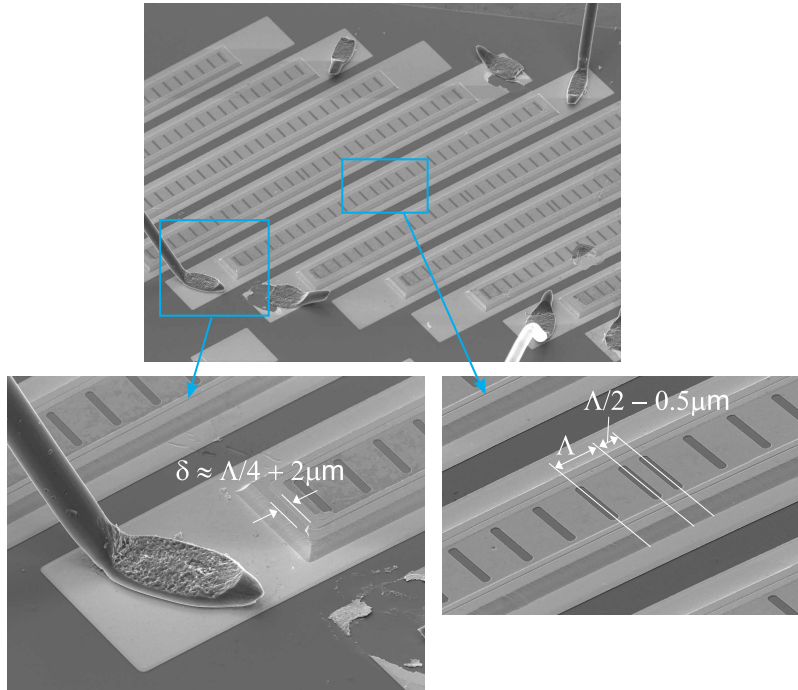
Fig. 9. SEMs of metal-metal grating devices fabricated with mesas along $\langle 100 \rangle$ directions. The sidewalls and facets are covered with 300/30/350 nm of SiO_2/Ti/Au. Al wire bonds are made on bonding pads away from the mesas to electrically bias the lasers. SiO_2 isolates the bonding pads from the bottom Ta/Cu.

(30/350 nm) deposition on sidewalls and facets, as well as to form bonding pads adjacent to bottom of the mesas. The outward sloped sidewalls and facets in this process allow this deposition to be done in a single lithography step. Before backside-metalization of the wafer, the substrate was thinned to 160 μm to improve heat-sinking. A die consisting several tens of such grating devices along with some Fabry-Perot ridge waveguides was then In-soldered on a Cu chip carrier and mounted for testing on a cold-plate in a vacuum cryostat. The emitted laser light was collected normal from the surface without any optical components inside the cryostat.

Figure 10(a) shows cw spectra from different surface-emitting grating devices within the range of grating-periods that were implemented on the fabrication-mask ($\Lambda = 28 - 32$ μm). The spectra were measured at 5 K using a Nicolet 850 spectrometer (purged with N_2 gas) with a room-temperature deuterated triglycine sulfate (DTGS) pyroelectric detector at a resolution of 0.125 cm^{-1} (= 3.75 GHz). Most devices tested, like the ones reported in Fig. 10(a), lased in single-mode for all bias-conditions, down to the instrument limited noise floor of 30 dB below maximum. There were, however, a few random devices that had additional modes which we attribute to lithography fluctuations. The lasing wavelength λ_0 scales linearly with grating period Λ as shown by the solid red line in Fig. 10(c). The line, however, does not cross origin since the mode index n_{eff} for cavities with metal-covered sidewalls changes with wavelength when the wavelength is comparable to the width. The dashed line in blue shows a line passing through origin corresponding to a n_{eff} value of 3.44 for the $\Lambda = 28$ μm device. For a device at a longer wavelength, n_{eff} ($\propto k_z$) will drop as the lateral component k_x increases, which explains the deviation of $\Lambda > 28$ μm grating devices from the dashed blue line. For the range of grating periods available on the mask, an operation range of ~ 0.35 THz is demonstrated for the single-
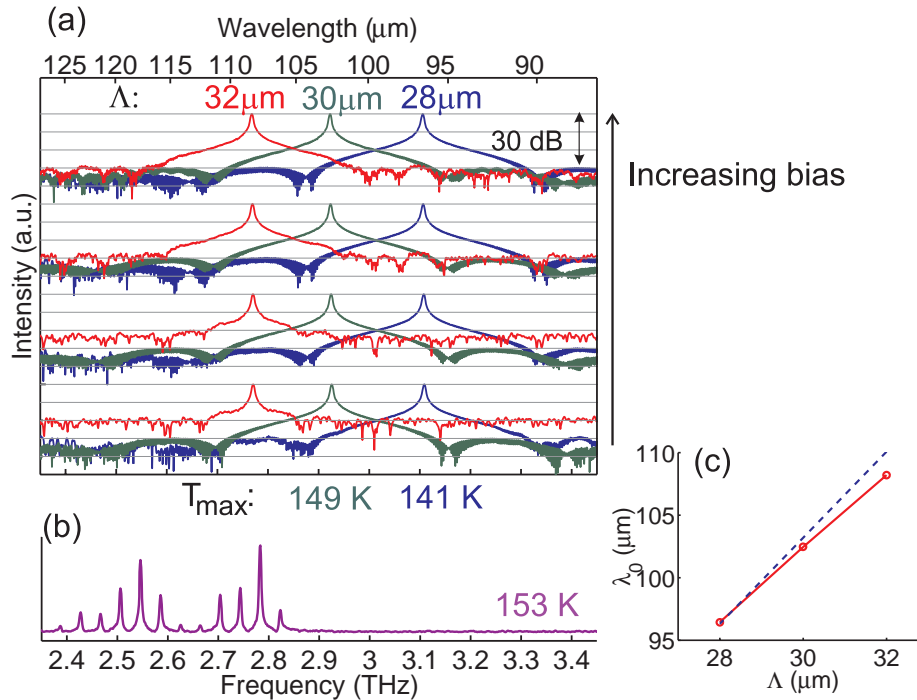
Fig. 10. (a) 5-K cw spectra for three different grating devices (each color corresponding to a device with different Λ), plotted on log scale. Spectra for different bias are plotted starting from near-threshold bias at bottom to peak-bias at top. Signal recorded from the $\Lambda = 32\,\mu m$ device, which lased at 2.77 THz, was very weak due to it being on a strong atmospheric water-absorption line. Maximum temperature of pulsed operation are also indicated. (b) CW spectrum from a Fabry-Perot ridge laser that was located adjacent to grating devices on the same die, plotted on linear scale. (c) λ_0 versus Λ variation (in solid red). A line going through origin and corresponding to $n_{\text{eff}} \approx \lambda_0/\Lambda = 3.44$ is also plotted (in dashed blue).

mode grating devices with this gain medium. The multi-mode spectrum for a Fabry-Perot edge-emitting laser from the same die shown in Fig. 10(b), however, indicates the possibility of accessing an even wider range.

Radiation patterns for grating devices were measured at 5 K with a Ge:Ga photo-detector in pulsed mode, and with a microbolometer camera in quasi-CW mode (25 % duty-cycle). Measurement results from the $\Lambda = 30\,\mu m$ device are shown in Fig. 11. The other two grating devices also had similar radiation patterns. This measurement was done with only a $\sim 300\,\mu m$ thick polypropylene dewar window in between the laser and the detector. A single-lobed pattern in the longitudinal (z) direction is observed as expected. The beam is relatively divergent in the lateral (x) direction due to a waveguide width that is of the order of the wavelength. In the far-field image of Fig. 11(a), a single-lobed pattern is observed in the lateral direction as well; however, the camera image in Fig. 11(b), which is taken from a much closer distance (due to a small camera size), shows two additional lobes which are likely due to evanescent field.

Figure 12 shows measured optical power versus current (L-I) characteristics for the $\Lambda = 30\,\mu m$ grating device in both pulsed and cw mode of operation. Light was collected without use of any cone optics. In pulsed operation, the device lased up to a maximum heat-sink temperature (T_{max}) of 149 K and the threshold current density (J_{th}) at 5 K was 460 A/cm^2. A temperature tuning of 19.7 GHz was observed for the single-mode spectrum from 5 K to 147 K. In cw
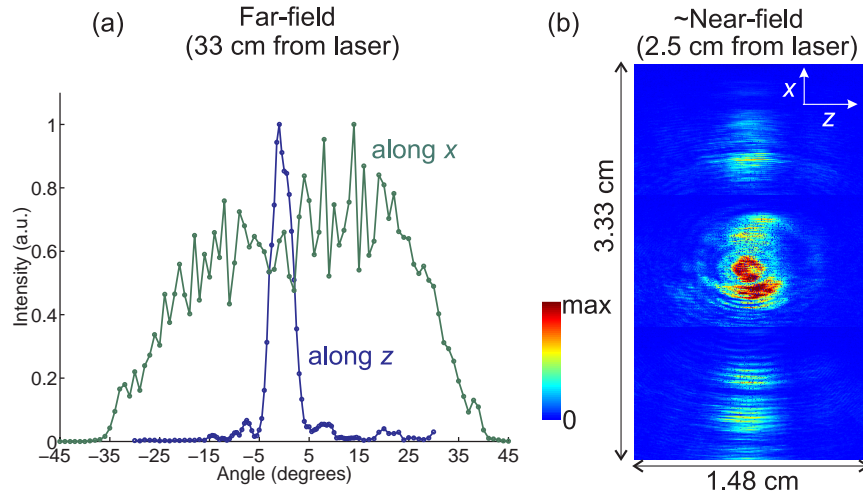
Fig. 11. (a) Far-field radiation pattern measured from the $\Lambda = 30\,\mu$m grating device with a He-cooled Ge:Ga photo-detector at an angular resolution of $< 1°$, and a distance of 33 cm from the laser. The full-width at half-maximum in the longitudinal (z) direction is $\sim 5°$. (b) Real-time snapshot of the radiation pattern at a distance of ~ 2.5 cm from the laser taken with a room-temperature 320×240 element (1.48×1.11 cm^2) microbolometer camera [6]. Three images taken at different x locations are stacked vertically to show the full image.

mode, the corresponding value for T_{max} was 78 K and J_{th} at 5 K was 560 A/cm^2. 6.1 mW of cw power was detected with a thermopile detector (Scientech, model AC2500) placed adjacent to the cryostat window. CW power per facet for the edge-emitting Fabry-Perot devices with comparable dimensions was typically smaller by a factor of ~ 2. The bottom panel of Fig. 12 also shows the measured cw voltage versus current (V-I) characteristics for the grating device. The negative differential-resistance (NDR) occurs at ~ 15 V beyond which the device stops lasing. Removal of the highly doped GaAs contact layer on top of the active region stack causes an extra 2–3 V drop to occur at the top metal-semiconductor Schottky contact, causing extra Joule heating in the grating devices and thus limiting their cw performance. However, the lasing dynamic range in current and hence the pulsed T_{max} remain unaffected.

L-I characteristics for the $\Lambda = 32\,\mu$m grating device could not be measured since it was lasing right on a strong atmospheric water absorption line. While the $\Lambda = 30\,\mu$m grating device lased up to 149 K in pulsed mode, the $\Lambda = 28\,\mu$m grating device lasing further away from the peak frequency of the gain spectrum (as deduced from the Fabry-Perot mode-spectrum of Fig. 8(c)) lased up to 141 K. For comparison, edge-emitting Fabry-Perot ridge lasers with metal on the sidewalls, measured from the same die as that of the grating devices, lased up to 153 K. It is likely that temperature performance of grating devices is slightly degraded due to non-uniform current injection on top because of metal gratings, and the lasing frequency is away from the gain peak. This suggests that the surface losses induced by the gratings for the parameters in this paper are comparable with the facet loss of the Fabry-Perot devices. Further adjustment of grating parameters, such as duty cycles, facet and defect lengths, could lead to much higher output power levels.

6. Conclusion

We have presented techniques for implementing second-order gratings in metal-metal waveguides to realize single-mode surface-emitting terahertz quantum-cascade lasers. For ter-
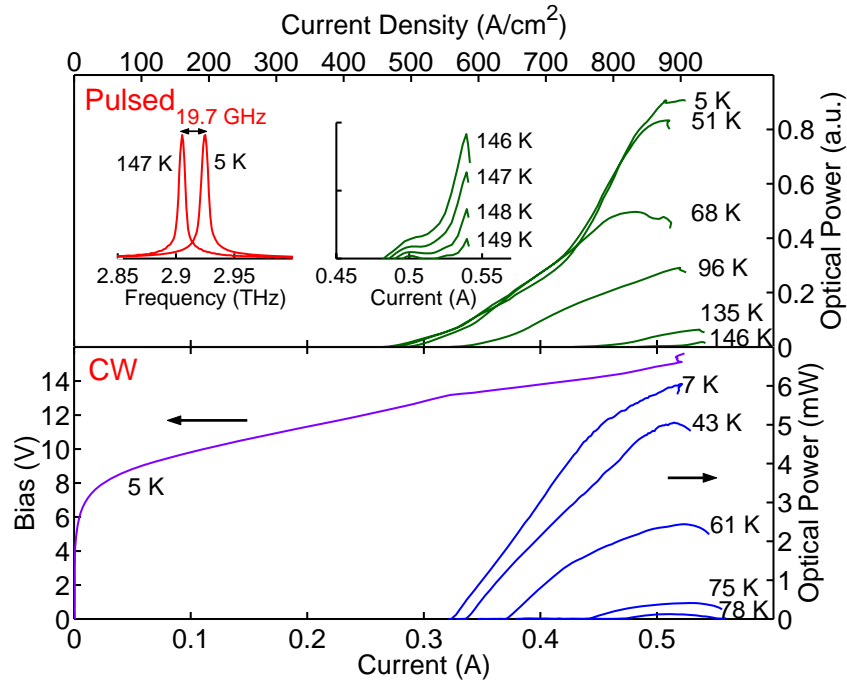
Fig. 12. Pulsed (top) and cw (bottom) *L-I* characteristics measured from the $\Lambda = 30$ μm grating device (ridge-size: 65 μm $\times$ 0.90 mm). The cw *I-V* measured at 5 K is also plotted. The pulsed data is taken using 200-ns pulses repeated at 10 kHz with a He-cooled Ge:Ga photo-detector, while the cw data is measured with room-temperature pyroelectric detector. The upper panel inset on the left shows temperature tuning of the single-mode spectrum due to change in the active region refractive index from 5 K to 147 K, while the inset on the right shows an expanded version of the *L-I*s at higher temperatures.

ahertz metal-metal waveguides, strong mode confinement leads to easy excitations of higher-order lateral modes. Because of the high facet reflectivities and strong grating coupling, device operation cannot be described by conventional coupled-mode theory. In this paper, the gratings are analyzed using finite-element simulations and design techniques are presented to control phase of reflection at the facets, which allows engineering of the mode shape inside the waveguide to achieve robust single-mode operation over a large frequency range. The implementation of a central defect has yielded single-lobed far-field radiation patterns. A fabrication scheme in which the mesas are formed at 45° angles to the substrate cleave directions allows outward sloped sidewalls in all directions by wet-etching. This has been used effectively to cover the cavity sidewalls with insulator/metal that helps to eliminate higher-order lateral modes. The ability to achieve robust-single mode operation while almost maintaining the temperature performance of Fabry-Perot devices, with relatively large amount of optical power and a good beam pattern, makes these lasers ideal for practical applications that are being targeted by terahertz quantum cascade lasers.

Acknowledgments